Low-temperature antiferromagnetic order in orthorhombic $CePdAl_3$

Vivek Kumar,[1,*] Andreas Bauer,[1,2] Christian Franz,[1,3] Jan Spallek,[1] Rudolf Schönmann,[1] Michal Stekiel,[1,3] Astrid Schneidewind,[3] Marc A. Wilde,[1,2] and C. Pfleiderer[1,2,4]

[1]*Physik-Department, Technische Universität München, D-85748 Garching, Germany*

[2]*Zentrum für QuantumEngineering (ZQE), Technische Universität München, D-85748 Garching, Germany*

[3]*Jülich Centre for Neutron Science (JCNS) at Heinz Maier-Leibnitz Zentrum (MLZ), D-85748 Garching, Germany*

[4]*Munich Center for Quantum Science and Technology (MCQST), Technische Universität München, D-85748 Garching, Germany*

(Received 31 December 2022; revised 26 April 2023; accepted 2 May 2023; published 12 June 2023)

We report the magnetization, ac susceptibility, and specific heat of optically float-zoned single crystals of $CePdAl_3$. In comparison to the properties of polycrystalline $CePdAl_3$ reported in the literature, which displays a tetragonal crystal structure and no long-range magnetic order, our single crystals exhibit an orthorhombic structure (*Cmcm*) and antiferromagnetic order below a Néel temperature $T_1 = 5.6$ K. The specific heat at zero field shows two anomalies, namely, a broad transition at $T_1 = 5.6$ K followed by a λ-anomaly at $T_2 = 5.4$ K. A conservative estimate of the Sommerfeld coefficient of the electronic specific heat, $\gamma = 121\ \mathrm{mJ\,K^{-2}\,mol^{-1}}$, indicates a moderately enhanced heavy-fermion ground state. A twin microstructure evolves in the family of planes spanned by the basal plane lattice vectors $\mathbf{a}_o$ and $\mathbf{c}_o$, with the magnetic hard axis $\mathbf{b}_o$ common to all twins. The antiferromagnetic state is characterized by a strong $\mathbf{a}_o$, $\mathbf{c}_o$ easy-plane magnetic anisotropy where the $\mathbf{a}_o$ direction is the easy axis in the easy plane. A spin-flop transition induced under magnetic field along the easy directions, results in complex magnetic phase diagrams. Taken together, our results reveal a high sensitivity of the magnetic and electronic properties of $CePdAl_3$ to its structural modifications.

DOI: 10.1103/PhysRevResearch.5.023157

I. INTRODUCTION

Cerium-based intermetallic compounds exhibit a variety of ground states and various physical phenomena, such as unconventional superconductivity [1–8], heavy-fermion states [9,10], non-Fermi-liquid behavior [11], vibronic hybrid excitations [12–16], and complex magnetic order [17–24]. On the phenomenological level, the origin of this remarkable diversity of ground states has been attributed to the competition of narrow *f*-electron bands and strong electronic correlations together with spin-orbit interactions, crystal electric field (CEF) effects, and strong magnetoelastic coupling. An overarching theme connecting much of the research in *f*-electron compounds concerns the conditions for the emergence of magnetic order.

A class of compounds with the general formula $CeTX_3$ (*T* is a transition metal and *X* is a *p*-block element) crystallizing in subgroups of the $BaAl_4$-type ($I4/mmm$) tetragonal structure has received special attention [3,6,22–44]. In these compounds, a large number of structural variants and diverse magnetic and electrical properties may be stabilized for different transition metals *T*. Many members of this class of materials such as $CeRhGe_3$, $CeAuAl_3$, $CeCuAl_3$, and $CeCoGe_3$ adopt a noncentrosymmetric tetragonal structure ($BaNiSn_3$-type $I4mm$) and exhibit antiferromagnetic behavior [25–33]. Other members such as $CeAgAl_3$ display ferromagnetism with a centrosymmetric orthorhombic crystal structure [34,35]. A spin-glass state was reported in noncentrosymmetric tetragonal $CePtAl_3$ below 0.8 K [32]. Complex magnetic phases have been observed in antiferromagnetic $CeNiGe_3$ [22,24], $CeCoGe_3$ [23,36–38,43], and $CePtSi_3$ [39]. The discovery of pressure-induced unconventional superconductivity in the noncentrosymmetric tetragonal heavy-fermion antiferromagnets $CeRhSi_3$, $CeIrSi_3$, $CeCoGe_3$, $CeIrGe_3$, and $CeRhGe_3$ even suggests a new direction in condensed matter physics [3,6,40–42].

An important aspect is the structural stability of these systems and the emergence of different electronic ground states. As one of the first examples, $CePd_2Al_2$ [13,15], which is closely related to the class of $CeTAl_3$ of materials, was found to undergo a structural phase transformation from a tetragonal to an orthorhombic lattice at 13.5 K. An inelastic neutron scattering study revealed three magnetic excitations in the paramagnetic phase. However, according to Kramer's theorem, only two CEF excitations are expected due to the splitting of ground state $J = 5/2$ of the Ce^{3+} ion into three doublets in tetragonal/orthorhombic point symmetry, suggesting strong coupling between the crystal fields and the crystal structure. Later, Adroja *et al.* found a similar anomaly in $CeCuAl_3$ [14], where a structural instability manifests itself in terms of a drastic change in lattice parameters of the tetragonal structure around 300 °C [29]. These anomalous excitations have been interpreted by means of Thalmeier and Fulde's model of bound states between phonons and CEF excitations as generalized to the tetragonal point symmetry. Recently, Čermák *et al.* confirmed related hybrid CEF-phonon

*vivek.kumar@tum.de

excitations even for weak magnetoelastic coupling in isostructural $CeAuAl_3$ [45]. Moreover, $CePd_2Al_2$, $CeCuAl_3$, and $CeAuAl_3$ order antiferromagnetically at low temperatures and exhibit incommensurate amplitude-modulated magnetic structures [15,46–48]. The presence of multistep magnetism and complex magnetic phase diagrams suggests the possible existence of topologically nontrivial multi-k structures akin to skyrmion lattices [49]. This raises the question of if and how the formation of magnetic order depends on the stabilization of specific crystal structure.

In this paper, we focus on $CePdAl_3$. A study of as-cast polycrystalline $CePdAl_3$ by Schank *et al.* in 1994 revealed a tetragonal structure with lattice constants $a = 4.343$ Å and $c = 10.578$ Å [50], where the heat treatment at high temperature results in a structural phase transformation and the emergence of antiferromagnetic order below 6 K. In contrast, no magnetic order was found down to 0.1 K in a recent investigation by Franz *et al.* on single-crystalline tetragonal $CePdAl_3$ grown by optical float zoning with a growth rate of 5 mm/h [51]. With this growth rate, only a few single-crystal grains were obtained. For the work reported in the following, a single crystal was prepared by optical float zoning using a much lower growth rate of 1 mm/h under the assumption that $CePdAl_3$ forms through a peritectic reaction [52]. Under these conditions, we obtained large single-crystal grains and found that $CePdAl_3$ crystallizes in an orthorhombic as opposed to a tetragonal structure. In this paper, we report comprehensive magnetization, ac susceptibility, and specific-heat measurements on single-crystalline orthorhombic $CePdAl_3$. As our main result, we find the characteristics of strongly anisotropic antiferromagnetic order below 5.6 K. We determine the magnetic phase diagram up to 14 T, where we find the emergence of complex magnetic phases under magnetic fields applied along the easy directions. The presence of different structural and magnetic configurations of $CePdAl_3$ identifies an example of a material in which to search for hybrid excitations and new magnetic phases in the future.

The paper is organized as follows. After a brief account of the experimental methods in Sec. II, we present our experimental results in Sec. III. We start with the structural properties and notation in Sec. III A, followed by the specific-heat results in Sec. III B and magnetic susceptibility data in Sec. III C. The temperature and field dependence of the magnetization are presented in Sec. III D. We find that the magnetic field-driven transitions for fields applied along the easy direction are consistent with the specific heat as a function of temperature at different fields as presented in Sec. III E. In Sec. III F, we examine the magnetic transitions in more detail by analyzing the hysteresis of the field-dependent magnetic susceptibility. Comprehensive datasets allow one to infer the magnetic phase diagram presented in Sec. III G. The conclusions are summarized in Sec. IV.

II. EXPERIMENTAL METHODS

A single crystal of $CePdAl_3$ was grown using the optical floating-zone technique following a process similar to that described in Refs. [51–54]. The crystal growth was performed using four 500 W halogen lamps under an argon atmosphere at a pressure of 2.5 bar. The seed and feed rods were rotated at 6 rpm in opposite directions. As the main difference to Ref. [51], the growth rate was reduced from 5 mm/h [51] to 1 mm/h [52], which resulted in the formation of an orthorhombic crystal.

The crystal structure of $CePdAl_3$ was determined by means of single-crystal x-ray diffraction (SCXRD). A platelet-shaped crystal with dimensions $50 \times 40 \times 10$ μm was cleaved of the $CePdAl_3$ crystal as grown. The platelet was investigated at a Rigaku XtaLAB Synergy-S diffractometer, using a Mo x-ray source with $\lambda = 0.71$ Å and a two-dimensional HyPix-Arc 150° detector. Bragg reflections were indexed using CRYSALIS PRO [55] as integrated with the diffractometer. The crystal structures of pieces taken from different parts of the float-zoned ingot were investigated using powder x-ray diffraction on a Huber G670 diffractometer.

The single crystals were oriented by Laue x-ray diffraction and a cuboidal sample was cut with orientations $\mathbf{a}^\star_o$, $\mathbf{c}^\star_o$, and $\mathbf{b}_o$ as introduced below for the measurement of the bulk properties. The ac susceptibility, magnetization, and specific heat were measured in a Quantum Design physical property measurement system (PPMS) at temperatures down to 2 K under magnetic fields up to 14 T. In order to determine the temperature dependence of the bulk properties, the sample was first cooled from a high temperature, well above the magnetic ordering temperature, to the lowest attainable temperature in the absence of a magnetic field. Subsequently, the field was set to the desired value and data were collected for increasing temperature. This protocol was repeated for different target magnetic fields. The ac susceptibility was measured at an excitation amplitude of 1 mT and an excitation frequency of 911 Hz. The specific heat was measured down to 2 K using a large heat-pulse method [56]. For temperatures between 0.08 and 4 K, the specific heat was measured in a Dryogenic adiabatic demagnetization refrigerator using a conventional heat-pulse method.

The field dependence of the magnetization and the ac susceptibility was measured using the following temperature versus field protocol. First, the sample was cooled from a high temperature well above the magnetic ordering temperature to the target temperature in the absence of a magnetic field. Second, data as a function of magnetic field were recorded in a sequence of field sweeps from zero field to 14 T, 14 to −14 T, and −14 to 14 T.

The bulk properties recorded on different pieces cut from the large single-crystal ingot were consistent. The temperature- and field-dependent features along $\mathbf{a}^\star_o$ and $\mathbf{c}^\star_o$ were qualitatively identical. Therefore, comprehensive data, focused on one of these directions, i.e., $\mathbf{c}^\star_o$, were recorded. Summarizing the key result of our study, the magnetic phase diagrams of $CePdAl_3$ were inferred. Signatures detected in measurements as a function of temperature and magnetic field are labeled as T_j and H_j, respectively. For clarity, the same subscript j is assigned to the transitions corresponding to the same line in the phase diagram.

III. EXPERIMENTAL RESULTS

A. Crystal structure and twinning

Different crystal growth conditions favor tetragonal ($I4mm$) [51] or orthorhombic crystal structures of $CePdAl_3$.

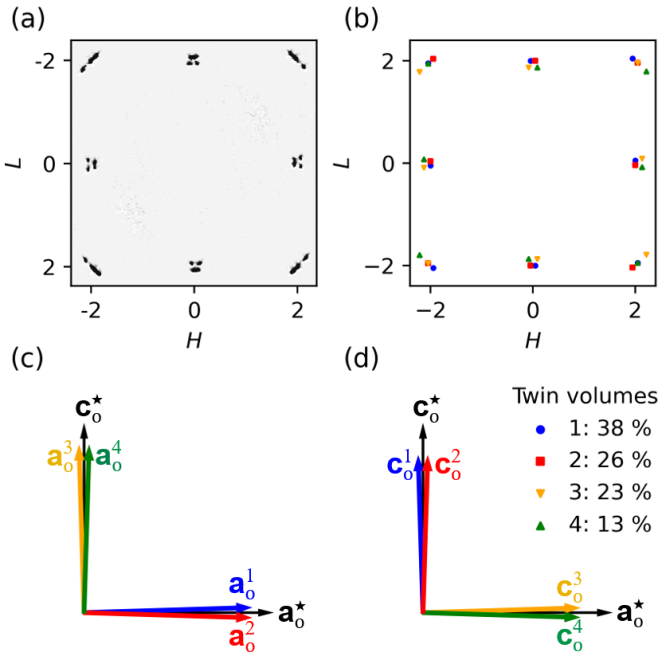

FIG. 1. Twin scheme in the basal plane of orthorhombic $CePdAl_3$ as derived from single-crystal x-ray diffraction. (a) X-ray scattering intensity reconstructed in the $H0L$ plane. The splitting of the reflections is characteristic of twin formation. (b) Indexed reflections of (a) with the colors corresponding to different twin domains. Schematics of the lattice vectors $\mathbf{a}_o^i$ and $\mathbf{c}_o^i$ of twin i in the basal plane $H0L$ of the orthorhombic crystal are depicted in (c) and (d). Four twins labeled $i = 1, 2, 3$, and 4 were identified. $\mathbf{a}_o^\star$ and $\mathbf{c}_o^\star$ are defined as mutual perpendicular sample directions comprising the admixtures of twin lattice vectors.

By means of single-crystal x-ray diffraction, we determined that the orthorhombic lattice stabilizes in the *Cmcm* space group. The lattice parameters at room temperature are $a_o = 6.379$ Å, $b_o = 10.407$ Å, and $c_o = 5.975$ Å. Measurements on pieces taken from different parts of the ingot exhibit the same orthorhombic structure. A diffractogram of the quenched final zone is characteristic of multiple structurally different phases, consistent with $CePdAl_3$ forming through a peritectic reaction. The observation of an orthorhombic crystal structure at low growth rate (1 mm/h, slow cooling) as compared to a tetragonal structure at a high growth rate (5 mm/h, fast cooling) suggests that those structures are thermodynamically stable at low and high temperatures, respectively. Fast cooling prevents the transition between those structures kinetically, realizing the tetragonal structure as a metastable state at ambient temperature.

The single-crystalline orthorhombic phase exhibits a pseudotetragonal twinning in the basal plane, evident, for instance, by the splitting of the Bragg reflections shown in Fig. 1(a). The twinning law was determined by indexing all measured reflections with components of the four twins presented in Fig. 1(b). An illustration of the twin orientation is shown in Figs. 1(c) and 1(d). The three perpendicular Cartesian directions of twins for $i = 1, 2, 3, 4$ are denoted by $\mathbf{a}_o^i$, $\mathbf{b}_o^i$, and $\mathbf{c}_o^i$, where $\mathbf{a}_o^i$ and $\mathbf{c}_o^i$ construct an effective basal plane and $\mathbf{b}_o^i$ mutually represent the long axis. The volume fraction of the four twins labeled $i = 1, 2, 3$, and 4 are 0.38, 0.26, 0.23, and 0.13, respectively. The mismatch angle between the twins numbered 1 and 2, as well as 3 and 4, is around 3°.

Measurements on different pieces cleaved from the single-crystalline ingot demonstrate the same twinning scheme with minor differences in twin fractions of different twins. An attempt to detwin the crystals by means of high-temperature treatment, etching, or cleaving of micrometer-sized crystals affected neither the twinning as such nor the twinning fractions.

In turn, measurements in any direction in the effective basal plane effectively reflect an admixture of $\mathbf{a}_o^i$ and $\mathbf{c}_o^i$ directions due to the four twins. We define, therefore, two mutually perpendicular effective *sample* directions $\mathbf{a}_o^\star$ and $\mathbf{c}_o^\star$, explicitly taking into account the volume fractions of the four twins. This definition is schematically depicted in Figs. 1(c) and 1(d), where $\mathbf{a}_o^\star$ is nearly aligned along $\mathbf{a}_o^{1,2}$ and $\mathbf{c}_o^{3,4}$, while $\mathbf{c}_o^\star$ is aligned to that of $\mathbf{c}_o^{1,2}$ and $\mathbf{a}_o^{3,4}$. The third crystal direction, corresponding to the long axis $\mathbf{b}_o$, remains unaffected by the twin deformations.

For tetragonal and orthorhombic samples of $CePdAl_3$, we obtained residual resistivities of 26 and 7 μΩcm, respectively. Such values are reasonable for Ce-based compounds. Although the direct comparison of residual resistivity values across different compounds is difficult, the reduced value of the orthorhombic sample may hint at a reduced amount of disorder.

B. Temperature dependence of the specific heat

The temperature dependence of the specific heat $C(T)$ is shown in Fig. 2 for single-crystalline tetragonal ($I4mm$) and orthorhombic ($Cmcm$) $CePdAl_3$ as well as nonmagnetic polycrystalline tetragonal ($I4mm$) $LaPdAl_3$. For tetragonal $CePdAl_3$, neither the electrical resistivity studied down to ∼0.1 K nor the magnetization measured down to 2 K provide any evidence of an ordering transition [51,57]. The upturn in the heat capacity below 5 K may be attributed to a Schottky anomaly associated with low-lying crystal electric fields. In orthorhombic $CePdAl_3$, a λ-type anomaly comprising a shoulder closely above the transition temperature $T_1 = 5.6$ K followed by a peak at $T_2 = 5.4$ K is observed, where the magnetization is characteristic of antiferromagnetism as reported below. The behavior observed is consistent with a previous study of polycrystalline $CePdAl_3$ [50]. Moreover, the properties are reminiscent of the commensurate-to-incommensurate magnetic transition reported for other strongly correlated systems [58,59].

A pronounced shoulder in the specific heat has also been seen in other systems, notably the chiral cubic magnet MnSi [56,60], where it reflects a change of character of the critical spin fluctuations when approaching long-range helimagnetic order and a concomitant fluctuation-induced first-order transition. We did not detect any hints suggestive of first-order transitions in the specific-heat data of orthorhombic $CePdAl_3$. Details of the low-temperature specific heat of orthorhombic $CePdAl_3$ at zero field are presented in Sec. III E, which also includes data collected at different magnetic fields.

Above T_1, the expression $C/T = \gamma + \beta T^2$, where γ and β are the electronic and phononic contributions to the

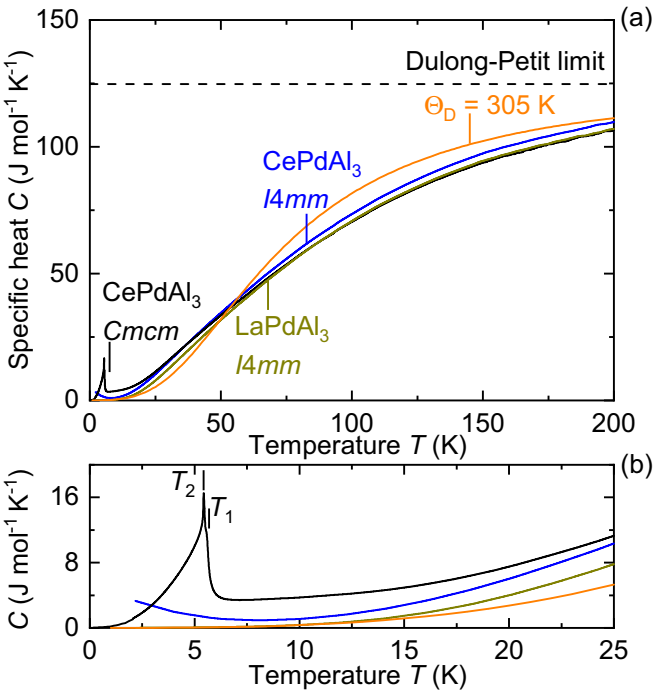

FIG. 2. (a) Zero-field specific heat of single-crystalline orthorhombic (black) and tetragonal (blue) [57] $CePdAl_3$ as a function of temperature. Data of orthorhombic $CePdAl_3$ were measured in a Dryogenic system between 0.08 and 4 K, and in a PPMS between 2 and 200 K. Also shown are the specific heat of nonmagnetic polycrystalline $LaPdAl_3$ (gray line) and the Debye fit (orange line) calculated from the low-temperature specific heat of the *Cmcm* structure. The Debye temperature is $\Theta_D = 305$ K. The Dulong-Petit limit for all three compounds, $15R = 124.7$ J mol^{-1} K^{-1}, is depicted by a dashed line. (b) The low-temperature part of the specific heat of orthorhombic $CePdAl_3$ shows a pronounced λ-type anomaly with a broad shoulder at $T_1 = 5.6$ K followed by a peak at $T_2 = 5.4$ K.

specific heat, respectively, has been fitted to the specific-heat data in the range ∼18 to ∼23 K of orthorhombic $CePdAl_3$. The values obtained for γ and β are 234 mJ mol^{-1} K^{-2} and 3.437×10^{-4} J mol^{-1} K^{-4}, respectively. The Debye temperature, $\Theta_D = 305$ K, associated with β may be derived using the relation $\beta = (12/5)\pi^4 nR/\Theta_D^3$, where n is the number of atoms per formula unit and R is the gas constant. Fitting the specific-heat data of $LaPdAl_3$ between 2 and 10 K yields $\gamma =$ 5 mJ mol^{-1} K^{-2} and $\beta = 2.957 \times 10^{-4}$ J mol^{-1} K^{-4}. The resulting Debye temperature, $\Theta_D = 320$ K, is consistent with the value obtained for orthorhombic $CePdAl_3$. The phonon contribution to the specific heat in the Debye model (orange line in Fig. 2) is given by

$$C_{\mathrm{ph,Debye}} = 9nR\left(\frac{T}{\Theta_D}\right)^3 \int_0^{x_D} \frac{x^4 e^x}{(e^x-1)^2} dx, \qquad (1)$$

where $x_D = \Theta_D/T$. At high temperatures, the experimental data of tetragonal $LaPdAl_3$ and $CePdAl_3$, as well as orthorhombic $CePdAl_3$, approach the Dulong-Petit limit, $3nR = 15R = 124.7$ J mol^{-1} K^{-1}, where $n = 5$. The data at intermediate temperatures do not follow the Debye model, suggesting an additional phononic contribution to the specific heat under the Einstein model. A simple consideration of splitting of the phonon spectrum into three acoustic and 12 ($= 3n - 5$) optical branches under the Debye and Einstein models, respectively, may lead to various possible sets of Debye and Einstein temperatures that can equally describe the phononic specific heat at intermediate as well as high temperatures. Hence, a fruitful explanation of the overall phononic specific heat will only be possible by measuring the phonon dispersion in the future.

The large value of $\gamma = 234$ mJ mol^{-1} K^{-2} obtained from the low-temperature specific heat above T_1 is typical for a heavy-fermion system. It has to be borne in mind, however, that evaluating γ at the relatively high temperatures above T_1 is associated with substantial uncertainties. A lower bound of γ, fitting the experimental data in the antiferromagnetic state at temperatures between ∼0.9 and ∼3.7 K, yields a value of $\gamma = 121$ mJ mol^{-1} K^{-2} still characteristic of heavy-fermion behavior.

At high temperatures ($T > 100$ K), the specific heat of all three compounds shown in Fig. 2(a) exhibits essentially the same temperature dependence. However, the specific heat of orthorhombic $CePdAl_3$ is slightly smaller than for tetragonal $CePdAl_3$, suggesting reduced electronic and phononic contributions associated with the reduced crystal symmetry. Compared to nonmagnetic tetragonal $LaPdAl_3$, the specific heat of orthorhombic $CePdAl_3$ is also slightly smaller, yet within the experimental error of experiment. Knowing that there is only a quantitative difference in the specific heats at high temperatures, the specific heat of $LaPdAl_3$ (*I*4*mm*) with a prefactor may therefore serve as a nonmagnetic reference for $CePdAl_3$ (*Cmcm*) despite the difference in their crystal structures. Indeed, a multiplication with a fraction of 0.99 to the total signal of $LaPdAl_3$ fully superimposes the data of $CePdAl_3$, as shown in Fig. 3(a), of C/T vs T. The corresponding difference in specific heats may be attributed to the magnetic contribution of the specific heat of orthorhombic $CePdAl_3$.

Shown in Fig. 3(b) is a sharp peak at $T = 5.4$ K in the magnetic contribution to the specific heat after subtraction of the phonon contribution, signaling the antiferromagnetic transition. In addition, a broad maximum around 30 K may be discerned as characteristic of a Schottky anomaly due to crystal electric field contributions.

In the tetragonal as well as the orthorhombic symmetry of the lattice, the degeneracy of the sixfold ground-state multiplet of the Ce^{3+} ion splits into three doublet states. These lift the first and second excited states with respect to the ground state, resulting in a contribution to the specific heat which can be expressed as [61]

$$C_{\mathrm{CEF}} = \frac{R}{Z}\sum_{l=0}^{2} g_l \left(\frac{E_l}{kT}\right)^2 \exp\left(-\frac{E_l}{kT}\right) - \frac{R}{Z^2}\left[\sum_{l=0}^{2} \frac{E_l}{kT} g_l \exp\left(-\frac{E_l}{kT}\right)\right]^2, \qquad (2)$$

where

$$Z = \sum_{l=0}^{2} g_l \exp\left(-\frac{E_l}{kT}\right) \qquad (3)$$

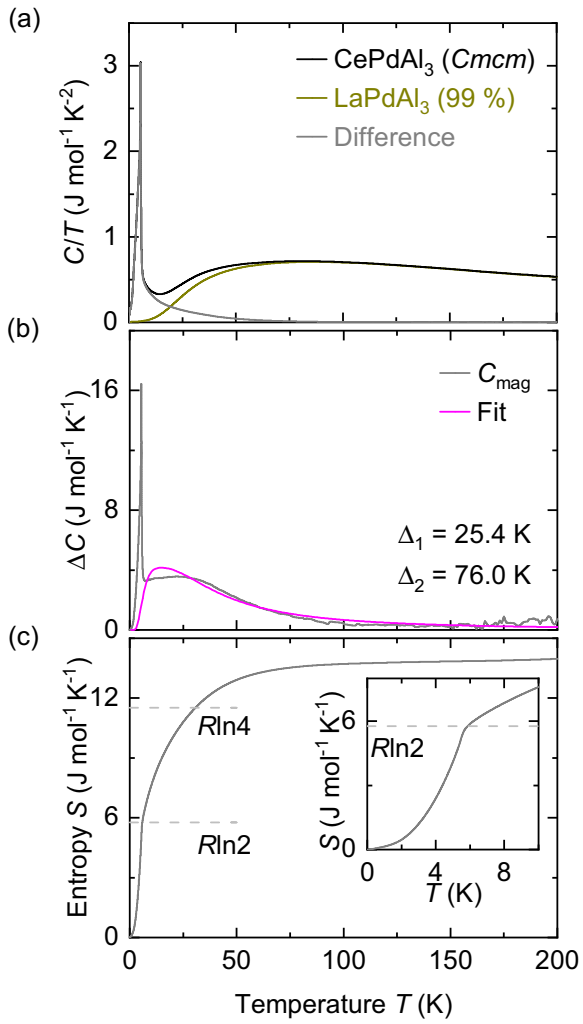

FIG. 3. Magnetic contribution to the specific heat and crystal electric field levels. (a) Specific heat per unit temperature, C/T, of orthorhombic $CePdAl_3$ and tetragonal $LaPdAl_3$ (with a multiplication of a fraction of 0.99) as well as their difference. (b) Magnetic specific heat, C_{mag}, and the fit to the expression for the crystal electric field contribution to the specific heat yields $\Delta_1 = 25.4$ K and $\Delta_2 = 76.0$ K. (c) Magnetic contribution to the entropy. The inset shows the entropy at low temperatures.

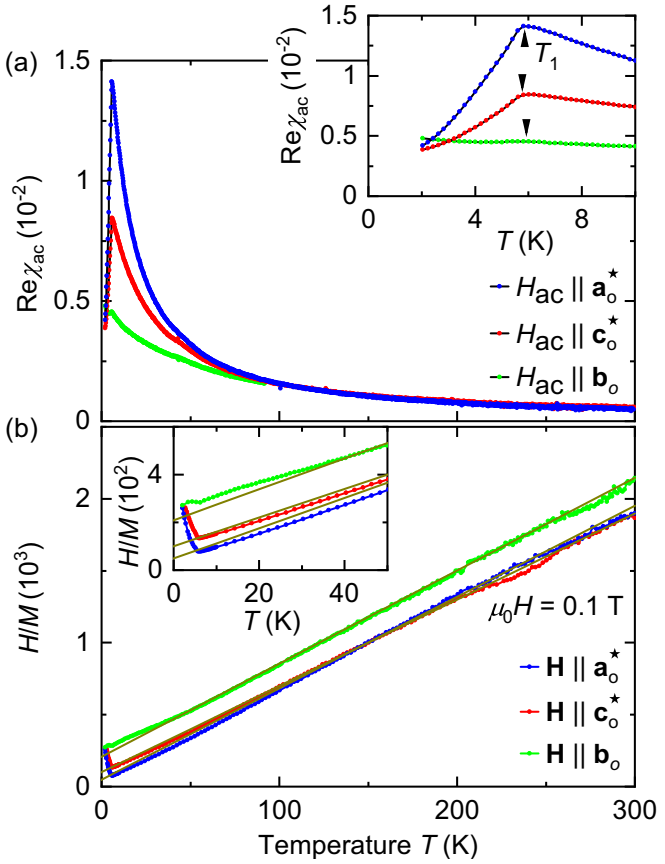

FIG. 4. (a) Temperature dependence of the real part of the ac susceptibility, $\mathrm{Re}\chi_{ac}$, of orthorhombic $CePdAl_3$ measured along $\mathbf{a}^\star_o$, $\mathbf{c}^\star_o$, and $\mathbf{b}_o$ at an excitation amplitude of 1 mT and a frequency of 911 Hz. The inset shows the low-temperature part of $\mathrm{Re}\chi_{ac}$, reflecting the characteristics of an antiferromagnetic transition at $T_1 = 5.6$ K. (b) Normalized inverse susceptibility, H/M, as a function of temperature for $\mathbf{H} \parallel \mathbf{a}^\star_o$, $\mathbf{H} \parallel \mathbf{c}^\star_o$, and $\mathbf{H} \parallel \mathbf{b}_o$ measured in a field of 0.1 T. Gray lines are Curie-Weiss fits. The inset shows the data for temperatures below 50 K.

is the partition function, and $l = 0$, 1, and 2 denote the ground, first, and second excited states, respectively. The degeneracy of the three doublet states is $g_0 = g_1 = g_2 = 2$.

The energy differences $E_1 - E_0 = \Delta_1$ and $E_2 - E_0 = \Delta_2$ represent the levels of the first and the second excited states, respectively. A fit of the data to Eq. (2) between 20 and 100 K yields $\Delta_1 = 25.4$ K and $\Delta_2 = 76.0$ K, respectively. Note that the normalized subtraction of the signal of $LaPdAl_3$ may introduce systematic errors in the determination of the precise values of the excited states. For instance, subtraction of the signal of $LaPdAl_3$ after multiplication with a fraction of 0.98 yields $\Delta_1 = 28.6$ K and $\Delta_2 = 95.5$ K.

Furthermore, we have calculated the magnetic entropy $S = \int (C/T)dT$ presented in Fig. 3(c). At the magnetic transition temperature, the entropy reaches the theoretical value of $R \ln 2$ for a doublet ground state expected of Ce^{3+} ions. When increasing the temperature, the entropy increases and reaches $R \ln 4$ around 30 K, approaching saturation above 100 K, which is consistent with the scheme of crystal electric field levels.

C. Temperature dependence of the magnetic susceptibility

The real part of the ac susceptibility, $\mathrm{Re}\chi_{ac}$, of orthorhombic $CePdAl_3$ as a function of temperature is shown in Fig. 4(a) for $\mathbf{a}^\star_o$, $\mathbf{c}^\star_o$, and $\mathbf{b}_o$. A clear magnetic transition is observed at $T_1 = 5.6$ K in the low-temperature range where T_1 coressponds to the value inferred from $C(T)$, characteristic of the onset of antiferromagnetic order, as indicated by arrows in the inset. Namely, below T_1, $\mathrm{Re}\chi_{ac}$ monotonically decreases along $\mathbf{a}^\star_o$ and $\mathbf{c}^\star_o$ with decreasing temperature, while slightly increasing along $\mathbf{b}_o$. The magnitude of $\mathrm{Re}\chi_{ac}$ along different axes differs significantly for $T < 100$ K, indicating sizeable magnetic anisotropy.

Figure 4(b) shows the normalized inverse susceptibility, H/M, as a function of temperature in a field of 0.1 T for $\mathbf{H} \parallel \mathbf{a}^\star_o$, $\mathbf{H} \parallel \mathbf{c}^\star_o$, and $\mathbf{H} \parallel \mathbf{b}_o$. In the paramagnetic state well above T_1,

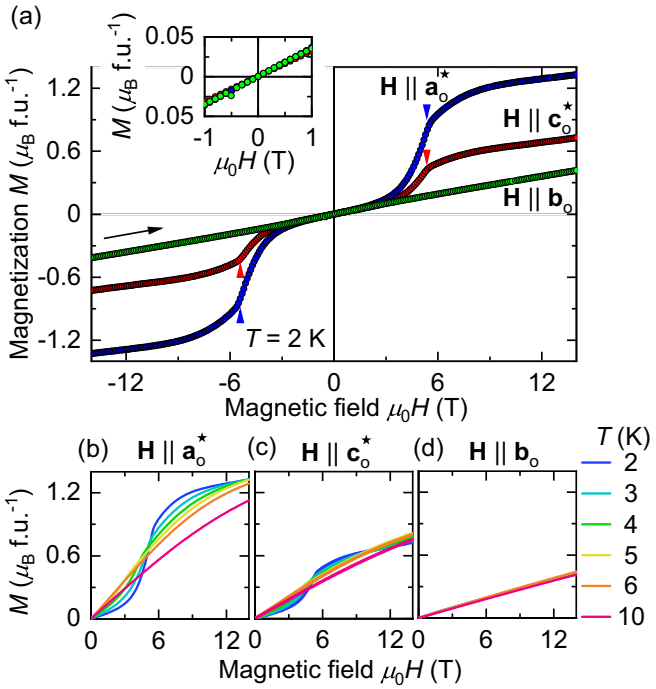

FIG. 5. (a) Isothermal magnetization of orthorhombic $CePdAl_3$ at 2 K measured in a magnetic field along $\mathbf{a}_o^\star$, $\mathbf{c}_o^\star$, and $\mathbf{b}_o$ up to 14 T. The arrow indicates the direction of increasing magnetic field. The inset shows the linear variation of the magnetization below 1 T. Typical field dependence of isothermal magnetization at various temperatures for (b) $\mathbf{H} \parallel \mathbf{a}_o^\star$, (c) $\mathbf{H} \parallel \mathbf{c}_o^\star$, and (d) $\mathbf{H} \parallel \mathbf{b}_o$. A spin-flop transition at ~5.5 T is observed below T_1 for $\mathbf{H} \parallel \mathbf{a}_o^\star$ (blue arrow) and $\mathbf{H} \parallel \mathbf{c}_o^\star$ (red arrow).

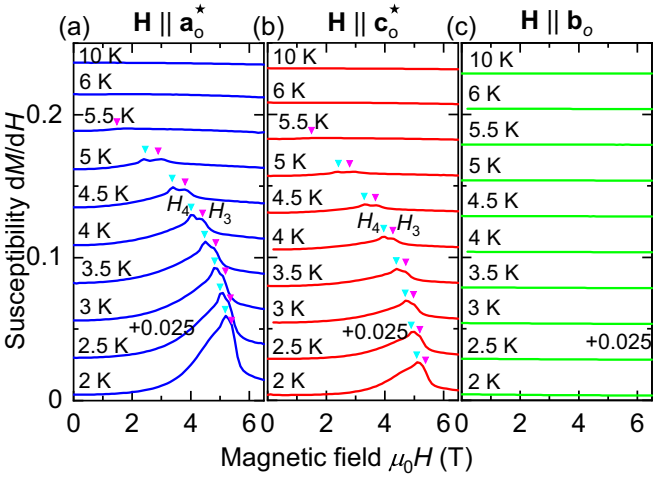

FIG. 6. (a) Susceptibility, dM/dH, calculated from the measured magnetization of orthorhombic $CePdAl_3$ for (a) $\mathbf{H} \parallel \mathbf{a}_o^\star$, (b) $\mathbf{H} \parallel \mathbf{c}_o^\star$, and (c) $\mathbf{H} \parallel \mathbf{b}_o$. Data are shifted by 0.025 for clarity. Peaks correspond to field-induced transitions marked by arrows at H_3 (pink) and H_4 (light blue). The peaks disappear above T_1.

a Curie-Weiss dependence is observed. A linear fit to the data above 100 K yields Weiss temperatures $\Theta_W^{a^\star} = -7.9 \pm 5.0$ K, $\Theta_W^{c^\star} = -16.8 \pm 1.9$ K, and $\Theta_W^{b} = -32.4 \pm 1.5$ K for $\mathbf{H} \parallel \mathbf{a}_o^\star$, $\mathbf{H} \parallel \mathbf{c}_o^\star$, and $\mathbf{H} \parallel \mathbf{b}_o$, respectively, characteristic of an antiferromagnetic coupling. Moreover, the effective moments of 2.44 ± 0.04, 2.51 ± 0.01, and 2.42 ± 0.02 μ_B per ion obtained under magnetic field along $\mathbf{a}_o^\star$, $\mathbf{c}_o^\star$, and $\mathbf{b}_o$, respectively, are close to the value of 2.54 μ_B expected for a free Ce^{3+} ion. This suggests a localized nature of the Ce moments in $CePdAl_3$. The deviation of H/M from the Curie-Weiss dependence for $T_1 < T < 100$ K shown in the inset of Fig. 4(b) may be related to CEF effects and electronic correlations. Furthermore, despite the twin deformations, a significant difference between the susceptibilities along $\mathbf{a}_o^\star$ and $\mathbf{c}_o^\star$ in the paramagnetic state indicates a large anisotropy in the basal plane, characteristic of an easy-plane system with an easy axis in the easy plane.

D. Magnetization

The magnetic field dependence of the isothermal magnetization of orthorhombic $CePdAl_3$ at 2 K for $\mathbf{H} \parallel \mathbf{a}_o^\star$, $\mathbf{H} \parallel \mathbf{c}_o^\star$, and $\mathbf{H} \parallel \mathbf{b}_o$ is shown in Fig. 5(a). No hysteresis is observed. The magnetization varies linearly in the low-field region up to 1 T, as shown in the inset of Fig. 5(a), consistent with antiferromagnetic order. For fields along $\mathbf{a}_o^\star$ and $\mathbf{c}_o^\star$, an S-shaped rise is observed in the magnetization when further increasing the field. A kink around 5.5 T suggests a field-driven transition. The magnetization values at 5.5 T are 0.85 μ_B for $\mathbf{H} \parallel \mathbf{a}_o^\star$, 0.44 μ_B for $\mathbf{H} \parallel \mathbf{c}_o^\star$, and 0.18 μ_B for $\mathbf{H} \parallel \mathbf{b}_o$. The magnetization increases monotonically above this transition where the moments along $\mathbf{a}_o^\star$ and $\mathbf{c}_o^\star$ at 14 T, the highest field strength studied, are 1.3 and 0.7 μ_B per Ce atom, respectively. In comparison, the magnetization increases linearly with the field for $\mathbf{H} \parallel \mathbf{b}_o$. The moment at 14 T is 0.4 μ_B per Ce atom.

Keeping in mind the twinned crystal structure, the magnetization along $\mathbf{a}_o^\star$ and $\mathbf{c}_o^\star$ represents a mixture of the crystallographic $\mathbf{a}_o$ and $\mathbf{c}_o$ axes. A large quantitative difference in the magnetization at 5.5 T along $\mathbf{a}_o^\star$ and $\mathbf{c}_o^\star$ makes it unlikely that a metamagnetic transition occurs at the same field value in the $\mathbf{a}_o$ and $\mathbf{c}_o$ directions in a single twin domain. Instead, it appears most likely that the increase in the magnetization corresponds to a spin flop in the $\mathbf{a}_o^i$ easy direction of each twin only.

Shown in Figs. 5(b)– 5(d) are the isothermal magnetization at various temperatures for $\mathbf{H} \parallel \mathbf{a}_o^\star$, $\mathbf{H} \parallel \mathbf{c}_o^\star$, and $\mathbf{H} \parallel \mathbf{b}_o$, respectively. The spin-flop transition in $M(H)$ for $\mathbf{a}_o^\star$ and $\mathbf{c}_o^\star$ shifts to lower fields under increasing temperature and vanishes above T_1. In contrast, the variation in $M(H)$ along $\mathbf{b}_o$ is essentially temperature independent in the antiferromagnetic state. This behavior is consistent with a hard magnetic $\mathbf{b}_o$ axis and an easy $\mathbf{a}_o$, $\mathbf{c}_o$ plane, where $\mathbf{a}_o$ is an easy axis in the easy plane.

In order to trace the field-driven magnetic transition, we have calculated the differential susceptibility, dM/dH, from the isothermal magnetization at various temperatures presented in Figs. 6(a)– 6(c) for $\mathbf{H} \parallel \mathbf{a}_o^\star$, $\mathbf{H} \parallel \mathbf{c}_o^\star$, and $\mathbf{H} \parallel \mathbf{b}_o$, respectively. For fields along $\mathbf{a}_o^\star$ and $\mathbf{c}_o^\star$, the transition is characterized by a broad peak at ~5.2 T at 2 K, which exhibits two peaks at elevated temperatures. These peaks exist below T_1, as marked by arrows at the transition fields H_3 and H_4, following the labeling scheme described in Sec. II. With increasing temperature, the field range between the peaks increases and both peaks shift to lower field values. No indica-

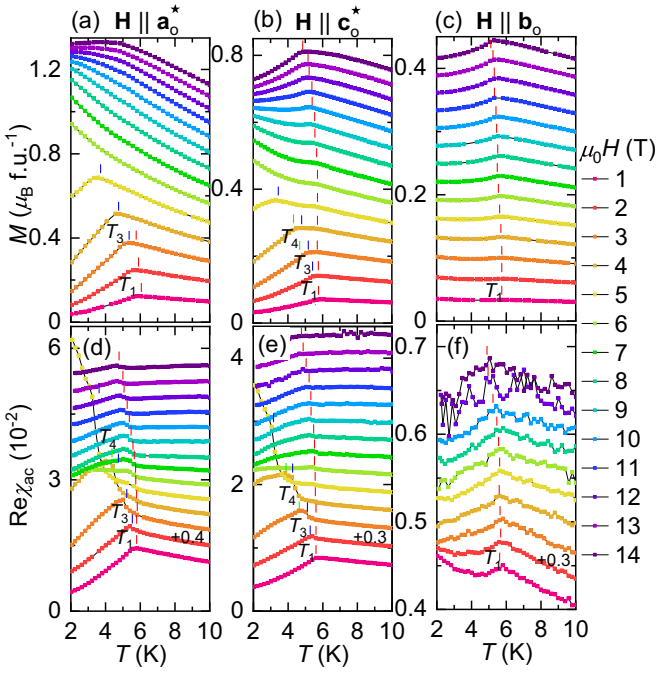

FIG. 7. Temperature dependence of the magnetization, $M(T)$, and the real part of the ac susceptibility, $\mathrm{Re}\chi_{ac}(T)$, of orthorhombic $CePdAl_3$ under magnetic fields up to 14 T. $M(T)$ is shown in (a)–(c) and $\mathrm{Re}\chi_{ac}(T)$ in (d)–(f) for $\mathbf{H} \parallel \mathbf{a}_o^\star$, $\mathbf{H} \parallel \mathbf{c}_o^\star$, and $\mathbf{H} \parallel \mathbf{b}_o$, respectively. $\mathrm{Re}\chi_{ac}(T)$ is shifted for clarity. Magnetic transitions are marked by vertical lines at temperatures T_1 (red), T_3 (blue), and T_4 (green). A complex behavior with multiple transitions is present for the field along $\mathbf{a}_o^\star$ and $\mathbf{c}_o^\star$ between 2 and 6 T.

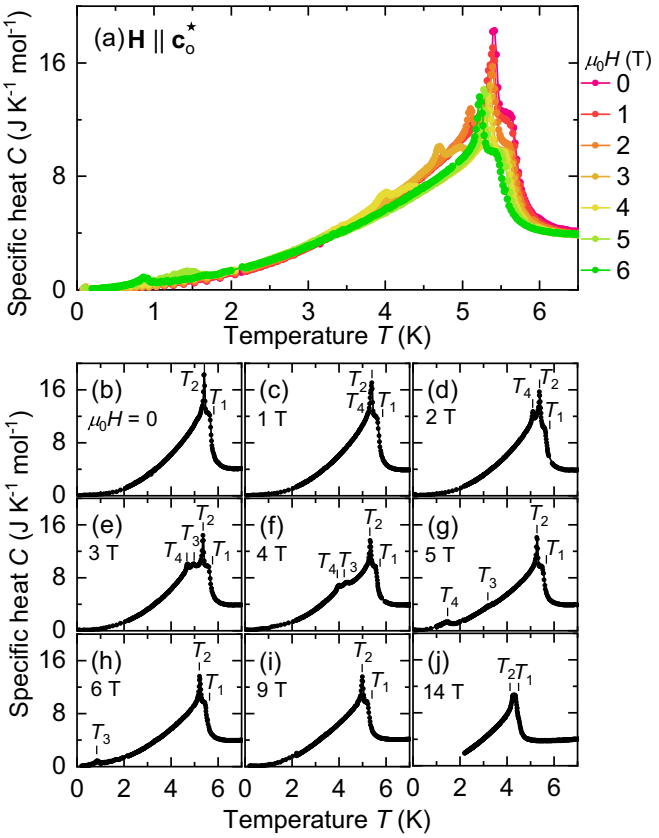

FIG. 8. Specific heat of orthorhombic $CePdAl_3$ as a function of temperature under selected magnetic fields up to 14 T applied along the $\mathbf{c}_o^\star$ axis. Data measured in the Dryogenic system between 0.08 and 4 K are combined with data measured in the PPMS above 2 K. At $H = 0$, the magnetic transition displays a broad shoulder with a point of inflection at T_1 followed by a peak at T_2. Additional peaks emerge at T_3 and T_4 for magnetic fields between 2 and 6 T.

tion exists of a field-induced transition in dM/dH for the field along $\mathbf{b}_o$.

The evolution of the field-induced transitions may be traced in further detail by the temperature dependence of the magnetization $M(T)$ and the ac susceptibility $\mathrm{Re}\chi_{ac}(T)$. Shown in Fig. 7 is $M(T)$ and $\mathrm{Re}\chi_{ac}(T)$ at various fields up to 14 T. By decreasing the temperature, orthorhombic $CePdAl_3$ undergoes a phase transformation from paramagnetism to antiferromagnetic order at a transition temperature T_1 (marked by red lines). This transition is visible in $\mathrm{Re}\chi_{ac}(T)$ in all crystallographic directions. The transition at T_1 shifts to lower temperatures under increasing field, but does not vanish up to the highest studied field of 14 T. In the intermediate field range from 2 to 6 T, clear changes in $M(T)$ and $\mathrm{Re}\chi_{ac}(T)$ for the field along $\mathbf{a}_o^\star$ [Figs. 7(a) and 7(d)] and $\mathbf{c}_o^\star$ [Figs. 7(b) and 7(e)] point to two additional phase transitions at temperatures denoted T_3 (blue line) and T_4 (green line). These transitions disappear at fields above 6 T. For $\mathbf{H} \parallel \mathbf{b}_o$, only the first transition at T_1 is observed in $M(T)$ and $\mathrm{Re}\chi_{ac}(T)$ [Figs. 7(c) and 7(f)].

E. Magnetic field dependence of the specific heat

The specific heat of orthorhombic $CePdAl_3$ as a function of temperature at different magnetic fields for $\mathbf{H} \parallel \mathbf{c}_o^\star$ is presented in Fig. 8. At zero magnetic field [Fig. 8(b)], a broad shoulder with a point of inflection is observed at T_1, followed by a sharp peak at T_2. Increasing the applied field results in a broadening of the peak at T_2 [Fig. 8(c)] and a splitting with an additional peak emerging at a lower temperature T_4. For even higher fields up to 6 T [Figs. 8(d)–8(h)], the position of T_4 continues to shift to lower temperatures with the emergence of another peak at T_3. The emergence of the peaks at T_3 and T_4 in the specific heat in the intermediate field range from 2 to 6 T is consistent with the phase transitions deduced from the magnetization and the ac susceptibility (see Figs. 6 and 7). For fields above 6 T, a noticeable shift of T_1 and T_2 to lower temperatures is observed.

F. Magnetic field dependence of the magnetic susceptibility

In order to investigate the qualitative difference between the transitions labeled as H_3 and H_4 in dM/dH (see Fig. 6), we have measured the magnetic susceptibility as a function of magnetic field between 0 and 14 T. Figure 9 shows the real part of the ac susceptibility, $\mathrm{Re}\chi_{ac}$, and the susceptibility calculated from the magnetization, dM/dH, as a function of increasing and decreasing field. At 2 K, dM/dH exhibits two peaks under increasing field, i.e., first, a pronounced peak at ∼5.2 T, followed by a second broad peak at ∼5.3 T for both $\mathbf{H} \parallel \mathbf{c}_o^\star$ [Figs. 9(a) and 9(d)] and $\mathbf{H} \parallel \mathbf{a}_o^\star$ [Figs. 9(c) and 9(f)]. The first peak shifts to ∼5.1 T, resulting in a hysteresis,

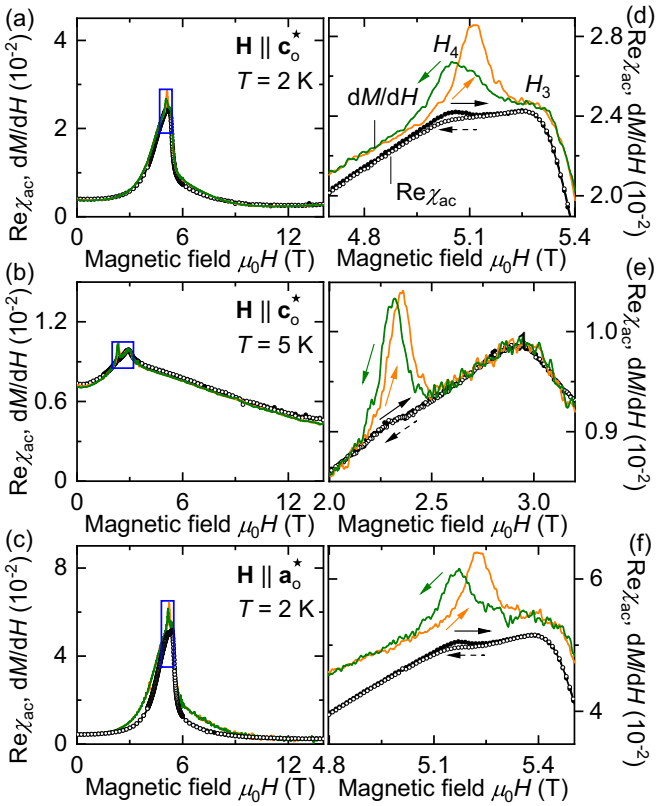

FIG. 9. Details of the magnetic transitions at H_3 and H_4. Shown are the real part of the ac susceptibility, $\mathrm{Re}\chi_{ac}$, and the susceptibility calculated from the magnetization, dM/dH, of orthorhombic $CePdAl_3$ as a function of increasing and decreasing field for (a) $\mathbf{H} \parallel \mathbf{c}_o^\star$ at 2 K, (b) $\mathbf{H} \parallel \mathbf{c}_o^\star$ at 5 K, and (c) $\mathbf{H} \parallel \mathbf{a}_o^\star$ at 2 K. (d)–(f) The magnetic transition regions corresponding to the blue rectangles in (a)–(c), respectively. Colors denote dM/dH for increasing (orange) and decreasing (green) magnetic field. Black circles correspond to $\mathrm{Re}\chi_{ac}$ for increasing (filled symbols) and decreasing (open symbols) field, respectively. dM/dH was calculated after smoothing the data.

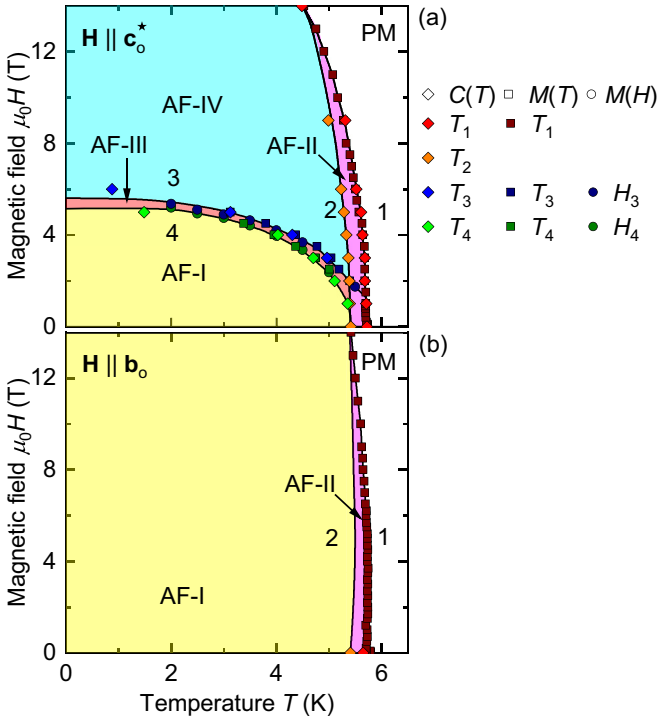

FIG. 10. Magnetic phase diagram of orthorhombic $CePdAl_3$ for (a) $\mathbf{H} \parallel \mathbf{c}_o^\star$ and (b) $\mathbf{H} \parallel \mathbf{b}_o$ as inferred from the magnetization and the specific heat. Due to crystal twinning, the phase diagram for $\mathbf{H} \parallel \mathbf{a}_o^\star$ qualitatively resembles the phase diagram for $\mathbf{H} \parallel \mathbf{c}_o^\star$ shown in (a). The characteristics of an easy magnetic plane are observed. Phase transitions are guided by the lines which are denoted by numerals $j = 1$, 2, 3, and 4. The associated temperature and field values are labeled as T_j and H_j, respectively. Four magnetically ordered phases may be distinguished, as discussed in the text.

while the second peak remains at the same field value under decreasing field. Similar effects exists in $\mathrm{Re}\chi_{ac}$, where the first peak becomes less pronounced with a smaller hysteresis and a slightly lower field of ∼5.1 T. Also, the value of $\mathrm{Re}\chi_{ac}$ is slightly lower around the transition. At higher temperatures, both peaks are shifted to lower field values. The hysteresis in $\mathrm{Re}\chi_{ac}$ decreases significantly and drops below the noise level at 5 K [Figs. 9(b) and 9(e)]. Here, the magnitude of $\mathrm{Re}\chi_{ac}$ matches well with dM/dH except around the first peak. The difference in character of the transitions labeled as H_3 and H_4 suggest an intrinsic origin, rather than being related to the twinned microstructure.

On the one hand, the hysteresis observed in dM/dH and $\mathrm{Re}\chi_{ac}$ is reminiscent of changes of population of a multidomain state. On the other hand, the smaller amplitude of $\mathrm{Re}\chi_{ac}$ as compared to dM/dH indicates the presence of slow relaxation processes around the phase transition. Similar features are known to trace spin textures such as helimagnetic disclination or skyrmions in magnetic materials [62–64]. Further experimental investigations are needed to explore such a possibility in orthorhombic $CePdAl_3$.

G. Magnetic phase diagram

Combining the features detected in the magnetization and the specific heat, we infer the magnetic phase diagrams for field parallel to $\mathbf{c}_o^\star$ and $\mathbf{b}_o$ shown in Figs. 10(a) and 10(b), respectively. Due to the twinned microstructure, the response of the magnetization, specific heat, and ac susceptibility are qualitatively alike for $\mathbf{H} \parallel \mathbf{a}_o^\star$ and $\mathbf{H} \parallel \mathbf{c}_o^\star$. In addition, the enhanced signal observed along $\mathbf{a}_o^\star$ as compared to $\mathbf{c}_o^\star$ indicates that $\mathbf{a}_o^\star$ reflects a larger fraction of the easy axis, $\mathbf{a}_o$. Therefore, the transitions along both $\mathbf{a}_o^\star$ and $\mathbf{c}_o^\star$ equally reflect the phenomenon associated with the easy $\mathbf{a}_o$ axis of the untwinned single domain. Taken together, the characteristics of an easy magnetic $\mathbf{a}_o$, $\mathbf{c}_o$ plane and a hard magnetic $\mathbf{b}_o$ axis are observed, where $\mathbf{a}_o$ is an easy axis.

Four magnetic regions may be distinguished for magnetic field along $\mathbf{c}_o^\star$, denoted AF-I, AF-II, AF-III, and AF-IV. At low temperature and zero field, the ground state is denoted as AF-I. With increase temperature, AF-II appears at 5.4 K followed by the paramagnetic (PM) state above 5.6 K. Signatures of the AF-II region are detected in the specific heat only. The application of a magnetic field at low temperature drives a spin-flop transition from AF-I to AF-IV with an intermediate region AF-III in a narrow field range only. For finite field applied along the hard axis, i.e., $\mathbf{H} \parallel \mathbf{b}_o$ [Fig. 10(b)], only the AF-I and PM phases were observed, possibly due to the

lack of specific-heat data for finite fields along the hard axis. However, the AF-II transition was observed in zero field and the AF-II regime is shown in the phase diagram in Fig. 10(b) for consistency.

While the magnetization suggests a collinear antiferromagnetic structure along $\mathbf{a}_o$ in the AF-I phase, and AF-IV shows the characteristics of a spin-flop phase, the nature of AF-II and AF-III remains unknown. Neutron scattering studies under magnetic field are needed to determine the nature of the four antiferromagnetic phases that we observed in the orthorhombic single-crystal $CePdAl_3$.

IV. CONCLUSIONS

In summary, we investigated the magnetization, ac susceptibility, and specific heat of single crystal $CePdAl_3$ grown by optical float zoning. A highly anisotropic behavior with a twinned orthorhombic crystal symmetry was observed. Antiferromagnetic order with Néel temperature $T_1 = 5.6$ K was observed in terms of transitions in the ac susceptibility and specific heat. The magnetization is characteristic of antiferromagnetic order with an easy $\mathbf{a}_o$, $\mathbf{c}_o$ plane where $\mathbf{a}_o$ direction represents the easy axis in the basal plane. Field-driven transitions were detected in the magnetization along the easy direction, consistent with the ac susceptibility and specific heat. Taken together, our study reveals a strong interplay of electronic correlations, complex magnetic order, and structural modifications in $CePdAl_3$.

ACKNOWLEDGMENTS

We wish to thank A. Engelhardt, S. Mayr, A. Deyerling, C. Oberleitner, and W. Simeth for fruitful discussions and assistance with the experiments. We thank T. E. Schrader for measurements with the Rigaku single-crystal diffractometer in the x-ray labs of the Jülich Centre for Neutron Science (JCNS). This study has been funded by the Deutsche Forschungsgemeinschaft (DFG, German Research Foundation) under TRR80 (From Electronic Correlations to Functionality, Project No. 107745057, Project E1, F2), SPP2137 (Skyrmionics, Project No. 403191981, Grant No. PF393/19), and DFG-GACR WI3320-13 (Project No. 323760292), the excellence cluster MCQST under Germany's Excellence Strategy EXC-2111 (Project No. 390814868). Financial support by the European Research Council (ERC) through Advanced Grants No. 291079 (TOPFIT) and No. 788031 (ExQuiSid) is gratefully acknowledged.

[1] E. Bauer, G. Hilscher, H. Michor, C. Paul, E.-W. Scheidt, A. Gribanov, Y. Seropegin, H. Noël, M. Sigrist, and P. Rogl, Heavy Fermion Superconductivity and Magnetic Order in Noncentrosymmetric $CePt_3Si$, Phys. Rev. Lett. **92**, 027003 (2004).

[2] T. Takeuchi, S. Hashimoto, T. Yasuda, H. Shishido, T. Ueda, M. Yamada, Y. Obiraki, M. Shiimoto, H. Kohara, T. Yamamoto *et al.*, Magnetism and superconductivity in a heavy-fermion superconductor, $CePt_3Si$, J. Phys.: Condens. Matter **16**, L333 (2004).

[3] N. Kimura, K. Ito, K. Saitoh, Y. Umeda, H. Aoki, and T. Terashima, Pressure-Induced Superconductivity in Noncentrosymmetric Heavy-Fermion $CeRhSi_3$, Phys. Rev. Lett. **95**, 247004 (2005).

[4] I. Sugitani, Y. Okuda, H. Shishido, T. Yamada, A. Thamizhavel, E. Yamamoto, T. D. Matsuda, Y. Haga, T. Takeuchi, R. Settai *et al.*, Pressure-induced heavy-fermion superconductivity in antiferromagnet $CeIrSi_3$ without inversion symmetry, J. Phys. Soc. Jpn. **75**, 043703 (2006).

[5] N. Kimura, Y. Muro, and H. Aoki, Normal and superconducting properties of noncentrosymmetric heavy fermion $CeRhSi_3$, J. Phys. Soc. Jpn. **76**, 051010 (2007).

[6] Z. Weng, M. Smidman, L. Jiao, X. Lu, and H. Yuan, Multiple quantum phase transitions and superconductivity in Ce-based heavy fermions, Rep. Prog. Phys. **79**, 094503 (2016).

[7] I. Bonalde, R. Ribeiro, W. Brämer-Escamilla, C. Rojas, E. Bauer, A. Prokofiev, Y. Haga, T. Yasuda, and Y. Ōnuki, Unusual behaviours and impurity effects in the noncentrosymmetric superconductor $CePt_3Si$, New J. Phys. **11**, 055054 (2009).

[8] C. Pfleiderer, Superconducting phases of *f*-electron compounds, Rev. Mod. Phys. **81**, 1551 (2009).

[9] N. Egetenmeyer, J. L. Gavilano, A. Maisuradze, S. Gerber, D. E. MacLaughlin, G. Seyfarth, D. Andreica, A. Desilets-Benoit, A. D. Bianchi, C. Baines *et al.*, Direct Observation of the Quantum Critical Point in Heavy Fermion $CeRhSi_3$, Phys. Rev. Lett. **108**, 177204 (2012).

[10] L. Jiao, M. Smidman, Y. Kohama, Z. Wang, D. Graf, Z. . Weng, Y. J. Zhang, A. Matsuo, E. D. Bauer, H. Lee, S. Kirchner, J. Singleton, K. Kindo, J. Wosnitza, F. Steglich, J. D. Thompson, and H. Q. Yuan, Enhancement of the effective mass at high magnetic fields in $CeRhIn_5$, Phys. Rev. B **99**, 045127 (2019).

[11] G. Stewart, Non-Fermi-liquid behavior in *d*-and *f*-electron metals, Rev. Mod. Phys. **73**, 797 (2001).

[12] P. Thalmeier and P. Fulde, Bound State between a Crystal-Field Excitation and a Phonon in $CeAl_2$, Phys. Rev. Lett. **49**, 1588 (1982).

[13] L. Chapon, E. Goremychkin, R. Osborn, B. Rainford, and S. Short, Magnetic and structural instabilities in $CePd_2Al_2$ and $LaPd_2Al_2$, Phys. B: Condens. Matter **378–380**, 819 (2006).

[14] D. T. Adroja, A. del Moral, C. de la Fuente, A. Fraile, E. A. Goremychkin, J. W. Taylor, A. D. Hillier, and F. Fernandez-Alonso, Vibron Quasibound State in the Noncentrosymmetric Tetragonal Heavy-Fermion Compound $CeCuAl_3$, Phys. Rev. Lett. **108**, 216402 (2012).

[15] M. Klicpera, M. Boehm, P. Doležal, H. Mutka, M. M. Koza, S. Rols, D. T. Adroja, I. Puente Orench, J. Rodríguez-Carvajal, and P. Javorsk, Magnetic structures and excitations in $CePd_2(Al,Ga)_2$ series: Development of the "Vibron" states, Phys. Rev. B **95**, 085107 (2017).

[16] C. Opagiste, R.-M. Galéra, M. Amara, C. Paulsen, S. Rols, and B. Ouladdiaf, Unconventional behavior of the $Ce_3Pt_{23}Si_{11}$ ferromagnet, Phys. Rev. B **84**, 134401 (2011).

[17] S. Takayanagi, H. Sato, T. Fukuhara, and N. Wada, Two magnetic transitions in $Ce_3Ir_4Sn_{13}$, Phys. B: Condens. Matter **199-200**, 49 (1994).

[18] H. Nakotte, E. Brück, K. Prokes, J. Brabers, F. De Boer, L. Havela, K. Buschow, and Y. Fu-ming, Complex antiferro-

magnetic order of CeCuSn, J. Alloys Compd. **207–208**, 245 (1994).

[19] A. Thamizhavel, R. Kulkarni, and S. K. Dhar, Anisotropic magnetic properties of $CeAg_2Ge_2$ single crystals, Phys. Rev. B **75**, 144426 (2007).

[20] T. Nakano, S. Onuma, N. Takeda, K. Uhlířová, J. Prokleška, V. Sechovsk, J. Gouchi, and Y. Uwatoko, Coexistence of localized and heavy itinerant states in antiferromagnetic $CePtGe_2$, Phys. Rev. B **100**, 035107 (2019).

[21] R. Settai, A. Misawa, S. Araki, M. Kosaki, K. Sugiyama, T. Takeuchi, K. Kindo, Y. Haga, E. Yamamoto, and Y. Onuki, Single crystal growth and magnetic properties of $CeRh_2Si_2$, J. Phys. Soc. Jpn. **66**, 2260 (1997).

[22] A. Das, L. Menon, A. Nigam, and S. Malik, Transport and magnetic studies on $CeNiGe_3$ compound, Phys. B: Condens. Matter **230–232**, 165 (1997).

[23] V. K. Pecharsky, O.-B. Hyun, and K. A. Gschneidner Jr., Unusual magnetic properties of the heavy-fermion compound $CeCoGe_3$, Phys. Rev. B **47**, 11839 (1993).

[24] A. P. Pikul, D. Kaczorowski, T. Plackowski, A. Czopnik, H. Michor, E. Bauer, G. Hilscher, P. Rogl, and Y. Grin, Kondo behavior in antiferromagnetic $CeNiGe_3$, Phys. Rev. B **67**, 224417 (2003).

[25] S. Mentink, N. Bos, B. Van Rossum, G. Nieuwenhuys, J. Mydosh, and K. Buschow, Antiferromagnetism and crystal-field effects in $CeCuX_3$ (X=Al,Ga) compounds, J. Appl. Phys. **73**, 6625 (1993).

[26] W.-H. Lee, M.-R. Yeh, D.-C. Wang, and F.-A. Yang, Competition between the screening effect and exchange interactions in the system $CeCu_{1-x}Al_{3+x}$ ($0 \leqslant x \leqslant 0.25$), Jpn. J. Appl. Phys. **33**, L424 (1994).

[27] O. Moze and K. Buschow, Crystal structure of $CeCuAl_3$ and its influence on magnetic properties, J. Alloys Compd. **245**, 112 (1996).

[28] S. Paschen, E. Felder, and H. Ott, Transport and thermodynamic properties of $CeAuAl_3$, Eur. Phys. J. B **2**, 169 (1998).

[29] M. Klicpera, P. Javorsk, S. Daniš, and T. Brunátová, Structural phase transition in $CeCuAl_3$ single crystal, Acta Phys. Pol. A **126**, 290 (2014).

[30] M. Klicpera, P. Javorsk, and M. Diviš, Magnetization and electrical resistivity measurements on $CeCuAl_3$ single crystal, J. Phys.: Conf. Ser. **592**, 012014 (2015).

[31] M. Kontani, H. Ido, H. Ando, T. Nishioka, and Y. Yamaguchi, Magnetic, transport and thermal properties of $CeCuAl_3$ single crystal, J. Phys. Soc. Jpn. **63**, 1652 (1994).

[32] S. Mock, C. Pfleiderer, and H. v. Löhneysen, Low-temperature properties of $CeTAl_3$ (T=Au, Cu, Pt) and $CeAuGa_3$, J. Low Temp. Phys. **115**, 1 (1999).

[33] A. D. Hillier, D. T. Adroja, P. Manuel, V. K. Anand, J. W. Taylor, K. A. McEwen, B. D. Rainford, and M. M. Koza, Muon spin relaxation and neutron scattering investigations of the noncentrosymmetric heavy-fermion antiferromagnet $CeRhGe_3$, Phys. Rev. B **85**, 134405 (2012).

[34] T. Muranaka and J. Akimitsu, Thermodynamic properties of ferromagnetic Ce-compound, $CeAgAl_3$, Physica C: Superconduct. Applic. **460–462**, 688 (2007).

[35] S. Nallamuthu, A. Dzubinska, M. Reiffers, J. R. Fernandez, and R. Nagalakshmi, Ferromagnetism in orthorhombic $RAgAl_3$ (R = Ce and Pr) compounds, Phys. B: Condens. Matter **521**, 128 (2017).

[36] A. Thamizhavel, T. Takeuchi, T. D Matsuda, Y. Haga, K. Sugiyama, R. Settai, and Y. Ōnuki, Unique magnetic phases in an antiferromagnet $CeCoGe_3$, J. Phys. Soc. Jpn. **74**, 1858 (2005).

[37] K. Kaneko, N. Metoki, T. Takeuchi, T. D. Matsuda, Y. Haga, A. Thamizhavel, R. Settai, and Y. Ōnuki, Multi-step magnetic transition in non-centrosymmetric compound $CeCoGe_3$, J. Phys.: Conf. Ser. **150**, 042082 (2009).

[38] M. Smidman, D. Adroja, A. D. Hillier, L. C. Chapon, J. W. Taylor, V. K. Anand, R. P. Singh, M. R. Lees, E. A. Goremychkin, M. M. Koza, V. V. Krishnamurthy, D. M. Paul, and G. Balakrishnan, Neutron scattering and muon spin relaxation measurements of the noncentrosymmetric antiferromagnet $CeCoGe_3$, Phys. Rev. B **88**, 134416 (2013).

[39] T. Kawai, Y. Okuda, H. Shishido, A. Thamizhavel, T. D. Matsuda, Y. Haga, M. Nakashima, T. Takeuchi, M. Hedo, Y. Uwatoko *et al.*, Magnetic and electrical properties in $CePtSi_3$ without inversion symmetry in the crystal structure, J. Phys. Soc. Jpn. **76**, 014710 (2007).

[40] H. Wang, J. Guo, E. D. Bauer, V. A. Sidorov, H. Zhao, J. Zhang, Y. Zhou, Z. Wang, S. Cai, K. Yang *et al.*, Anomalous connection between antiferromagnetic and superconducting phases in the pressurized noncentrosymmetric heavy-fermion compound $CeRhGe_3$, Phys. Rev. B **99**, 024504 (2019).

[41] T. Terashima, Y. Takahide, T. Matsumoto, S. Uji, N. Kimura, H. Aoki, and H. Harima, Fermi surface and superconductivity in noncentrosymmetric $CeRhSi_3$, Phys. Rev. B **76**, 054506 (2007).

[42] T. Kawai, M. Nakashima, Y. Okuda, H. Shishido, T. Shimoda, T. D. Matsuda, Y. Haga, T. Takeuchi, M. Hedo, Y. Uwatoko *et al.*, Pressure effect of electronic states in antiferromagnets $CeTX_3$ (T: Transition Metal, X: Si and Ge), J. Phys. Soc. Jpn. **76**, 166 (2007).

[43] A. Das, R. Kremer, R. Pöttgen, and B. Ouladdiaf, Magnetic ordering in $CeCoGe_3$, Phys. B: Condens. Matter **378–380**, 837 (2006).

[44] M. Stekiel, P. Čermák, C. Franz, W. Simeth, S. Weber, E. Ressouche, W. Schmidt, K. Nemkovski, H. Deng, A. Bauer *et al.*, Incommensurate antiferromagnetic order in $CePtAl_3$, Phys. Rev. Res. **5**, 013058 (2023).

[45] P. Čermák, A. Schneidewind, B. Liu, M. M. Koza, C. Franz, R. Schönmann, O. Sobolev, and C. Pfleiderer, Magnetoelastic hybrid excitations in $CeAuAl_3$, Proc. Natl. Acad. Sci. USA **116**, 6695 (2019).

[46] M. Klicpera, P. Javorsk, P. Čermák, A. Schneidewind, B. Ouladdiaf, and M. Diviš, Neutron scattering study of magnetic order in single-crystalline $CeCuAl_3$, Phys. Rev. B **91**, 224419 (2015).

[47] M. Matsumura, Y. Kawamura, M. Yoshina, T. Nishioka, and H. Kato, ^{27}Al-NQR study in $BaNiSn_3$-type $CeCuAl_3$, J. Phys.: Conf. Ser. **150**, 042122 (2009).

[48] D. T. Adroja, C. de la Fuente, A. Fraile, A. Hillier, A. Daoud-Aladine, W. Kockelmann, J. W. Taylor, M. M. Koza, E. Burzurí, F. Luis, J. I. Arnaudas, and A. delMoral, Muon spin rotation and neutron scattering study of the noncentrosymmetric tetragonal compound $CeAuAl_3$, Phys. Rev. B **91**, 134425 (2015).

[49] S. Mühlbauer, B. Binz, F. Jonietz, C. Pfleiderer, A. Rosch, A. Neubauer, R. Georgii, and P. Böni, Skyrmion lattice in a chiral magnet, Science **323**, 915 (2009).

[50] C. Schank, F. Jährling, L. Luo, A. Grauel, C. Wassilew, R. Borth, G. Olesch, C. Bredl, C. Geibel, and F. Steglich, 4f-conduction electron hybridization in ternary CeTMAl compounds, J. Alloys Compd. **207–208**, 329 (1994).

[51] C. Franz, A. Senyshyn, A. Regnat, C. Duvinage, R. Schönmann, A. Bauer, Y. Prots, L. Akselrud, V. Hlukhyy, V. Baran *et al.*, Single crystal growth of CeTAl$_3$ (T = Cu, Ag, Au, Pd and Pt), J. Alloys Compd. **688**, 978 (2016).

[52] R. Schönmann, *Single Crystal Growth and Low Temperature Properties of Non-centrosymmetric Cerium Systems*, Master's thesis, Technische Universität München, Garching, Germany, 2015.

[53] A. Neubauer, J. Bœuf, A. Bauer, B. Russ, H. v. Löhneysen, and C. Pfleiderer, Ultra-high vacuum compatible image furnace, Rev. Sci. Instrum. **82**, 013902 (2011).

[54] A. Bauer, A. Neubauer, W. Münzer, A. Regnat, G. Benka, M. Meven, B. Pedersen, and C. Pfleiderer, Ultra-high vacuum compatible induction-heated rod casting furnace, Rev. Sci. Instrum. **87**, 063909 (2016).

[55] CRYSALISPRO Software System, ver. 1.171.42.49, Agilent Technologies UK, Ltd., Oxford, United Kingdom (2022).

[56] A. Bauer, M. Garst, and C. Pfleiderer, Specific Heat of the Skyrmion Lattice Phase and Field-Induced Tricritical Point in MnSi, Phys. Rev. Lett. **110**, 177207 (2013).

[57] C. Franz, Investigation of quantum phase transitions in the absence of inversion symmetry, Ph.D. thesis, Technische Universität München, Garching, Germany, 2014.

[58] S. Mishra, A. Demuer, D. Aoki, and I. Sheikin, Specific heat of $CeRhIn_5$ in high magnetic fields: Magnetic phase diagram revisited, Phys. Rev. B **103**, 045110 (2021).

[59] N. Kumar, S. K. Dhar, A. Thamizhavel, P. Bonville, and P. Manfrinetti, Magnetic properties of $EuPtSi_3$ single crystals, Phys. Rev. B **81**, 144414 (2010).

[60] S. M. Stishov, A. E. Petrova, S. Khasanov, G. K. Panova, A. A. Shikov, J. C. Lashley, D. Wu, and T. A. Lograsso, Magnetic phase transition in the itinerant helimagnet MnSi: Thermodynamic and transport properties, Phys. Rev. B **76**, 052405 (2007).

[61] P. Lethuillier and J. Chaussy, Sign change of the CEF parameters in light rare earth compounds in relation with the delocalization of the 4f shell, J. Phys. **37**, 123 (1976).

[62] A. Bauer and C. Pfleiderer, Magnetic phase diagram of MnSi inferred from magnetization and ac susceptibility, Phys. Rev. B **85**, 214418 (2012).

[63] A. Bauer, A. Chacon, M. Wagner, M. Halder, R. Georgii, A. Rosch, C. Pfleiderer, and M. Garst, Symmetry breaking, slow relaxation dynamics, and topological defects at the field-induced helix reorientation in MnSi, Phys. Rev. B **95**, 024429 (2017).

[64] Y. Tokunaga, X. Yu, J. White, H. M. Rønnow, D. Morikawa, Y. Taguchi, and Y. Tokura, A new class of chiral materials hosting magnetic skyrmions beyond room temperature, Nat. Commun. **6**, 7638 (2015).